

Landscapes and nonequilibrium fluctuations of eukaryotic gene regulation

Masaki Sasai,^{1,2,*} Bhaswati Bhattacharyya,³ Shin Fujishiro,¹ and Yoshiaki Horiike³

¹*Fukui Institute for Fundamental Chemistry, Kyoto University, Kyoto 606-8103, Japan*

²*Department of Complex Systems Science, Nagoya University, Nagoya 464-8603, Japan*

³*Department of Applied Physics, Nagoya University, Nagoya 464-8603, Japan*

(Dated: February 17, 2025)

Understanding the interplay among processes that occur over different timescales is a challenging issue in the physics of systems regulation. In gene regulation, the timescales for changes in chromatin states can differ from those for changes in the concentration of product protein, raising questions about how to understand their coupled dynamics. In this study, we examine the effects of these different timescales on eukaryotic gene regulation using a stochastic model that describes the landscapes and probability currents of nonequilibrium fluctuations. This model shows that slow, nonadiabatic transitions of chromatin states significantly impact gene-regulation dynamics. The simulated circular flow of the probability currents indicates a maximum entropy production when the rates of chromatin-state transitions are low in the intensely nonadiabatic regime. In the mildly nonadiabatic regime, this circular flow fosters hysteresis, suggesting that changes in chromatin states precede changes in transcription activity. Furthermore, calculations using a model of a circuit involving three core genes in mouse embryonic stem cells illustrate how multilayer regulation of chromatin, or deep epigenetic regulation, can flexibly tune fluctuations in individual genes. These findings highlight the rich effects of nonadiabatic chromatin-state transitions on gene regulation in eukaryotic cells.

I. INTRODUCTION

The coupling of processes with different rates or different timescales is ubiquitous in regulation mechanisms of natural and artificial systems [1–6]. Gene regulation is an example of such coupling; the gene activity, or the rate at which the product protein concentration varies, depends on how the chromatin state is modified at different rates. To understand the effects of the rate difference between changes in the protein concentration and the chromatin state, we define the adiabaticity parameter,

$$\omega = \frac{\text{rate of the chromatin-state change}}{\text{rate of the protein-concentration change}},$$

$$= \frac{\text{timescale of the protein-concentration change}}{\text{timescale of the chromatin-state change}}.$$
(1)

Using an analogy from condensed-matter physics, we refer to the system as adiabatic when $\omega > 1$ and nonadiabatic when $\omega < 1$ [7, 8].

The difference between adiabatic and nonadiabatic limits can be explained concisely using a landscape picture, which illustrates system dynamics as the movements of the system over landscapes that represent stationary distributions. In the nonadiabatic limit of $\omega \ll 1$, transitions of chromatin between the active and inactive states are infrequent enough to treat the two chromatin states separately. For example, when the chromatin state is kept active (or inactive) with a Poissonian process of protein synthesis, the probability distribution

$P(p)$ that cells exhibit the product protein concentration p in each chromatin state should approach a stationary Gaussian-like distribution. The landscape defined by $U(p) = -\log P(p)$ then forms a parabola. After the probability distribution becomes stationary, there remain nonequilibrium fluctuations seen in the dynamic system's trajectories over the landscapes. In the nonadiabatic limit, these fluctuations are diffusion over each parabola associated with infrequent jumps between two parabolas (Fig. 1A). In the adiabatic limit of $\omega \gg 1$, on the other hand, the chromatin-state transitions are so frequent that the landscape is effectively averaged between the two states; the fluctuations are diffusion over this averaged landscape (Fig. 1B). It is interesting to examine

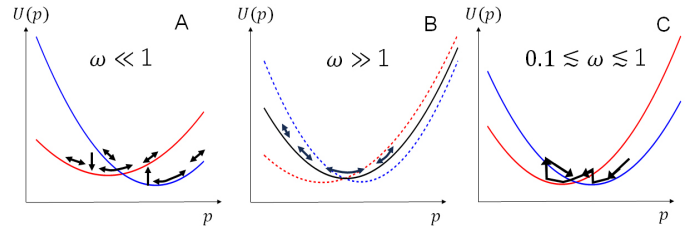


FIG. 1. Landscapes explaining the gene expression dynamics. (A) In the nonadiabatic limit of $\omega \ll 1$, the two chromatin states are separately described by the active-state landscape (blue) and the inactive-state landscape (red), and the system dynamics are diffusion over each landscape and the infrequent jumps between two landscapes. (B) In the adiabatic limit of $\omega \gg 1$, the active and inactive states are averaged to give rise to the averaged landscape (black). Dynamics are diffusion over this averaged landscape. (C) In the mildly nonadiabatic case of $0.1 \lesssim \omega \lesssim 1$, the frequency of jumps and the diffusion rate are comparable, showing an eddy of probability flow.

* masakiasai@nagoya-u.jp

the mildly nonadiabatic regime of $0.1 \lesssim \omega \lesssim 1$, where the rates of transitions and diffusion are comparable, showing the complex pattern of dynamic trajectories (Fig. 1C). This complex movement was referred to as “eddy” [8], which was systematically analyzed with a perturbation theory [9] and an exactly solvable model [10]. While the diffusive movements in the cases of $\omega \ll 1$ and $\omega \gg 1$ resemble fluctuations in equilibrium, simplistic analogies to equilibrium are invalid in the regime of $0.1 \lesssim \omega \lesssim 1$; therefore, we expect the nonequilibrium features of the gene-switching dynamics to be most evident in this eddy regime.

In Fig. 1, we illustrated the coupled dynamics of chromatin-state change and the protein-concentration change using multiple landscapes corresponding to multiple discrete states of chromatin. By interpreting the transitions between these discrete states of chromatin as changes in continuous variables, and by considering an extended landscape that encompasses both chromatin-state changes and protein-concentration changes, the eddy dynamics can be represented as probability currents over this extended landscape [11–13]. This extended landscape approach provides a physically intuitive description of the eddy dynamics, which we also adopt in the present study.

In studies of bacterial cells, the concept of an adiabatic limit has been widely applied [14]. This adiabatic framework is based on the assumption that the rapid binding/unbinding of transcription factors (TFs) to/from chromatin (≈ 10 s) [15] determines the chromatin state. The timescale for changes in protein concentration is comparable to the cell cycle period ($\approx 10^3$ s) [16], leading to a ratio of $\omega \approx 100$, which was thought to validate the adiabatic limit assumption [14]. However, several intriguing nonadiabatic phenomena have been observed in bacterial systems. For example, comparing Fig. 1A and Fig. 1B suggests that the number of basins in the landscape increases as ω decreases. This trend has been confirmed through experimental manipulations of the binding lifetime of λ -repressor [17] and tet-repressor [18] on bacterial chromatin. Moreover, nonadiabatic effects on cell-fate decisions have been emphasized in *Bacillus subtilis* [19]. In *E. coli* cells, single-cell measurements have shown that bursting transitions between active and inactive transcription occur on a timescale of 10^2 to 10^3 s [20]. These bursting transitions suggest that not only the rapid TF binding/unbinding but also the slower structural changes in chromatin play a role in chromatin-state transitions. This leads to a mild adiabaticity in the range of $1 \lesssim \omega \lesssim 10$, challenging the conventional assumption of an adiabatic limit. Therefore, it is essential to carefully examine the concepts of adiabaticity and nonadiabaticity in bacterial systems.

Nonadiabaticity is evident in eukaryotic cells, where changes in chromatin states occur due to slow epigenetic modifications of histones. These modifications take place over the course of several cell cycles [21, 22], with a typical cell cycle period of about $10 \sim 20$ h. In eu-

karyotic cells, protein concentrations often change due to biochemically regulated active degradation that proceeds on a timescale shorter than a cell cycle [23, 24], leading to a ratio of $\omega \approx 0.1$. As a result, eukaryotic genes are typically nonadiabatic [13, 17, 25–28]. Consequently, in these cells, the eddy dynamics can have a significant impact on gene switching and subsequent cell-fate decisions [13, 25, 26]. To better understand this phenomenon, a comprehensive analysis using various experimental and theoretical approaches is required. In this study, we take a step toward this goal by investigating the physical principles underlying the eddy dynamics through a model of eukaryotic gene circuits. We extend the previously developed model for a single eukaryotic gene [13] to encompass circuits composed of multiple genes.

To apply this model to cellular issues, we need to recognize that the chromatin state is regulated through multiple mechanisms in eukaryotic cells, including various types of histone modifications and the structural organization of chromatin at different spatial scales. An important question is why chromatin is regulated through such multiple coexisting mechanisms. We address this issue by applying the model to the problem of fluctuations in gene switching in mouse embryonic stem (mES) cells. Our findings suggest that the multilayered regulation of the interconnected redundant processes—which we refer to as deep epigenetic regulation—can work together to flexibly manage fluctuations in the activity of individual genes.

II. A PHYSICAL MODEL OF EUKARYOTIC GENE REGULATION

In this section, we present a model of eukaryotic gene regulation that emphasizes the differences in timescales between transitions in chromatin state and changes in protein concentration. The chromatin state of the i th gene in the circuit is described using the variables x_i and y_i . Here, x_i represents the binding status of TFs on the gene’s enhancer, while y_i represents the chemical modifications of histones within the chromatin domain that contains the enhancer and promoter of the i th gene. The protein concentration is denoted as p_i . See Fig. 2 for the model scheme.

We utilize the adiabatic approximation to derive the TF-binding state x_i , as explained in the subsection “Variables and parameters in the model.” Therefore, the variables we focus on in our integration of the equations of nonadiabatic dynamics are the histone state y_i and the protein concentration p_i .

TABLE I. Parameters in the model of eukaryotic gene regulation

Parameters explored in a wide range		values	references/notes
Adiabaticity	ω	$10^{-3} \leq \omega \leq 10^2$	$\omega \sim r_i^{yy'}/k \sim 0.1$ from the estimation of $r_i^{yy'}$ and k .
Typical concentration	\bar{p}	$0 < \bar{p} < 10$	$\xi_{11} = \bar{p}$ when the TF an activator. $\xi_{01} = \bar{p}$ when the TF is a repressor.
Other parameters		values	references/notes
Rate constant of protein degradation	k	1	$1/k$ is used as the unit of time. $k \sim 10^{-1} \text{ h}^{-1}$ [23, 24]
Rate of protein synthesis at the chromatin state xy	g_{xy}	$g_{xy} = \xi_{xy} k \Omega$	ξ_{xy} is given in Table II.
Volume surrounding chromatin	Ω	10^2	typical copy number of the protein $\approx \bar{p} \Omega$
Ratio of (binding-rate)/(unbinding-rate) of TF	h/f	$h_0 p^2/f$ (<i>Circuit A</i>) $h_0 p_i^2/f$ (<i>Circuit B</i>) $h_0 p_1 p_2/f, h_1 p_1 p_3^2/f$ (<i>Circuit C</i>)	Values of h_0/f and h_1/f are in Table II, which were chosen to make $h \approx f$ when $p_i = \bar{p}$. $f \sim 10^{-1} - 10^0 \text{ s}^{-1}$ [29, 30]
Histone-state transition rate from y' to y of the i th gene	$r_i^{yy'}$	$r_i^{yy'} = \omega_i \bar{r}^{yy'}$ (Eq. 2) $\bar{r}^{yy'} = \mu^{yy'} + \gamma^{yy'} x_i$ (Eq. 3)	$\mu^{yy'}$ and $\gamma^{yy'}$ are given in Table II. $r_i^{yy'} \sim 10^{-2} \text{ h}^{-1}$ [21, 22]

A. Variables and parameters in the model

1. Protein synthesis and degradation

The i th gene produces a protein at a rate of g_{xy} , resulting in the protein concentration p_i . The produced protein is degraded with the timescale of $1/k \sim 10^4 \text{ s}$ [23, 24]; here, we consider $1/k$ as a typical timescale to vary p_i .

In the present model, protein production is described as a stochastic process based on the following considerations: (1) In eukaryotic cells, mRNA is transcribed with bursting reactions [31–33], but the bursting timescale of $10^2 \sim 10^3 \text{ s}$ [33] is shorter than $1/k$. Therefore, we consider transcription to be a continuous stochastic process within our relevant timescale of $1/k$ as a first approximation. We will consider transcription bursting explicitly later in the “Deep epigenetic regulation” section (Sec. V) in this paper. (2) Processes of mRNA editing, export, and translation, which are involved in protein production, should have shorter timescales than $1/k$. (3) We focus on sufficiently small proteins that can pass through the nuclear pore without significant delay. Based on these points (1), (2), and (3), we adopt a simplified description of protein production as a single-step process occurring at the rate g_{xy} . In this notation, the indices x and y represent the chromatin state: $x = 1$ (or $x = 0$) when the TF binds to (or unbinds from) the enhancer of the gene, and $y = 1$ (or $y = -1$) when the histone state in the chromatin domain containing the gene is active (or inactive). The rate constants used in our model, along

with other parameters, are summarized in Table I.

We define the volume of the region containing the chromatin domain of interest as Ω . Given a typical protein concentration \bar{p} as $\bar{p} = g_{11}/(k\Omega)$ when the TF acts as an activator and $\bar{p} = g_{01}/(k\Omega)$ when the TF acts as a repressor, we anticipate that the protein concentration p_i will fall within the range $0 \leq p_i \lesssim \bar{p}$. As the typical protein concentration \bar{p} significantly influences behaviors of gene circuits, we will explore a range of values for \bar{p} in this study.

2. TF binding and unbinding

The binding status of a specific TF on the enhancer of the i th gene is denoted as x_i , which plays a crucial role in determining the probability of forming the transcription-initiation complex and the resulting protein-synthesis rate $g_{x_i y_i}$. We write $x_i = 1$ when the TF is bound on the enhancer and $x_i = 0$ when unbound. Then, $g_{1y} > g_{0y}$ when the TF is an activator and $g_{1y} < g_{0y}$ when the TF is a repressor.

We denote the binding rate of the TF to the enhancer as $h(q)$, with q being the TF concentration, and the unbinding rate as f . To examine the dynamic effects of the gene on circuit performance, we consider a scenario where x_i is not maintained to 1 or 0. This is facilitated by frequent and alternating binding and unbinding events with $h \approx f$. As a result, the timescale for binding, represented by $1/h$, is similar to the timescale for unbinding, $1/f$. This timescale determines the TF’s binding lifetime on chromatin, which has been estimated to be $1/f = 1 \sim$

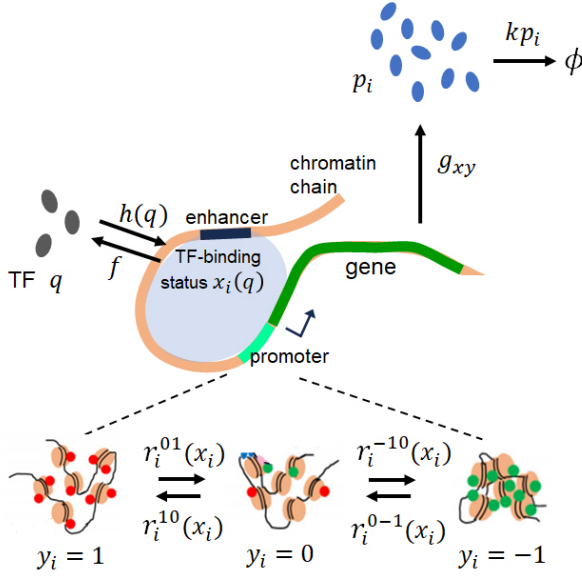


FIG. 2. A model of eukaryotic gene regulation. The enhancer of an example gene, indexed by i , binds a specific transcription factor (TF) with a concentration denoted as q at a rate $h(q)$ and unbinds it at a rate f . The gene produces a protein with a concentration p_i , which degrades with a rate constant k . The likelihood of TFs binding to the gene's enhancer is represented by $x_i(q)$. Chemical modifications of histones in the chromatin domain that contains the gene's enhancer and promoter are denoted as y_i . Processes such as the formation of the transcription-initiation complex (depicted in gray), bursting transcription, translation, and transport are combined into a single process characterized by a rate denoted as g_{xy} . The rate $r_i^{yy'}$ of change from one histone state y_i to another state y_i' is a function of x_i , denoted as $r_i^{yy'}(x_i)$. The model can be further extended to include cases where multiple TFs with concentrations $\{q\} = q_1, q_2, \dots$ bind to the enhancer of the gene.

10 s [29, 30]. Therefore, the timescales of binding and unbinding are significantly shorter than the timescale for changes in protein concentration, $1/k \sim 10^4$ s. The rapid transitions in TF binding and unbinding allow for the use of the adiabatic approximation, leading to the effective equilibration of x_i . We use the average value of x_i in this effective equilibrium as $x_i = h/(f + h)$ and regard x_i as a continuous variable of $0 \leq x_i \leq 1$ [14].

In scenarios where the system includes multiple transcription factors (TFs), we define their concentrations as $\{q\} = q_1, q_2, \dots$. When the j th TF binds to the enhancer of the i th gene, we denote the binding rate as $h^{ij} = h^{ij}(q_j)$ and the unbinding rate as f^{ij} . The binding state of the j th TF on the enhancer of the i th gene is represented by $x^{ij}(q_j)$. The adiabatic approximation allows us to express this as $x^{ij}(q_j) = h^{ij}/(f^{ij} + h^{ij}(q_j))$. In this study, we consider that all the activator TFs bound to the enhancer of gene i are essential for expressing that gene, resembling the behavior of an AND gate. Therefore, we define the TF-binding state of the i th gene as

$x_i = x_i(\{q\}) = \prod_j x^{ij}(q_j)$. Although the model can be applied to other scenarios, such as OR, NOR, and others, we use AND gates in the current study as examples to examine the effects of nonadiabaticity in gene regulation.

3. Chemical modifications of histones

The variable y_i represents whether the chemical modification of histones in a chromatin domain to which the i th gene belongs is of the active ($y_i = 1$) or inactive ($y_i = -1$) type. As transitions in the histone state are slower than changes in the protein concentration, we explore the nonadiabatic dynamics of y_i explicitly in the current model.

In many eukaryotic genomes, sub-megabase regions of the chromatin chain are condensed into domains. These domains are functional units that bear characteristic histone modification patterns depending on the activity of genes belonging to the domain [34]. The chemical modifications of histones in the domain significantly affect the degree of chromatin domain condensation; domains in the inactive histone state are more condensed than domains in the active histone state [35]. The degree of domain condensation determines the accessibility of RNA polymerase and related large-sized factors to DNA [36]. Thus, the histone modification pattern y of the domain crucially affects the protein-synthesis rate as $g_{x-1} \ll g_{x1}$.

We define the parameters $\bar{r}^{yy'}$ of the order of k to characterize transitions of histone states. Then, the transition rate $r_i^{yy'}$ from one domain-wide histone state y' to the other y at the i th gene is defined as

$$r_i^{yy'} = \omega_i \bar{r}^{yy'}. \quad (2)$$

Here, $r_i^{yy'}$ is explicitly scaled by the adiabaticity parameter ω_i , showing $r_i^{yy'} = O(\omega_i k)$. Although individual nucleosomes in eukaryotic cells are replaced on the timescale of hours, the interacting nucleosomes within a domain cooperatively change their histone modification patterns on the timescale of days [37–40], leading to $\omega_i \approx 0.1$. While this eddy-regime value ($0.1 \lesssim \omega_i \lesssim 1$) of the adiabaticity seems natural for eukaryotic cells, we explore a wider range of ω_i values in the present study, including both strongly adiabatic ($\omega_i \gg 1$) and strongly nonadiabatic ($\omega_i \ll 1$) cases, to highlight dynamics in the eddy regime.

Thus, we examine the circuit dynamics by varying the parameters \bar{p} and ω_i , while other parameters are fixed to plausible values as experimentally suggested or chosen for simplicity in our simulations as explained in Tables I and II.

4. Coupling between the histone and TF-binding states

The binding and unbinding rates, represented by h and f , determine the TF-binding state x_i . In the current

model, we focus on scenarios where h or f does not explicitly depend on the condensation level of the chromatin chain y_i . This lack of dependence is expected when the size of the TFs is sufficiently small, as seen in the case of pioneer factors [41]. However, the relationship between y_i and x_i is significant, as transitions in y_i are influenced by x_i as explained below.

The chromatin chain that interacts with activating TFs (activators) recruits histone acetylases. These enzymes alter histone modifications to create an active chromatin state. Conversely, the actions of histone methyltransferases become dominant on the chromatin chain associated with repressive TFs (repressors), which convert the histone modifications to an inactive state [42, 43]. Thus, the normalized rates $\bar{r}^{yy'}$ and rates $r_i^{yy'}$ of histone-state transitions depend on the TF-binding status x_i as $\bar{r}^{yy'}(x_i)$ and $r_i^{yy'}(x_i)$. To simplify this, we apply a first-order approximation regarding the dependence on x_i . Using coefficients $\mu^{yy'} \geq 0$ and $\gamma^{yy'}$ of the order of k , we write:

$$\bar{r}^{yy'}(x_i) = \mu^{yy'} + \gamma^{yy'} x_i. \quad (3)$$

When the TF is an activator, coefficients for activating transitions are $\gamma^{10} \approx \gamma^{0-1} > 0$ and those for inactivating transitions are $\gamma^{-10} \approx \gamma^{01} < 0$. When the TF is a repressor, $\gamma^{yy'}$ has the opposite sign as $\gamma^{10} \approx \gamma^{0-1} < 0$ and $\gamma^{-10} \approx \gamma^{01} > 0$. Values of $\mu^{yy'}$ and $\gamma^{yy'}$ used in the current study are summarized in Table II.

Once those $\mu^{yy'}$ and $\gamma^{yy'}$ are given, the adiabaticity parameter ω_i determines how the histone-state transition rate $r_i^{yy'}(x_i)$ depends on the TF-binding state x_i through Eqs. 2 and 3. Since the protein concentration p_i depends on both x_i and y_i via the protein-synthesis rate $g_{x_i y_i}$, Eqs. 2 and 3 explain how p_i responds to changes in x_i indirectly through the changes in y_i . This indirect response is expected to manifest as a delayed feedback effect, as observed in the heterochromatin bistability in yeast cells [44].

B. System dynamics

In a previous publication [13], we derived the Langevin equations for the dynamics of p and y of a single gene by interpreting both p and y to be continuous variables with $0 \leq p$ and $-1 \leq y \leq 1$. These equations were derived by representing their master equations in a path-integral form and applying the saddle-point approximation to them. Then, the landscape of p and y , which we call the extended landscape encompassing both the protein-concentration change and the chromatin-state change, was derived to describe their coupled dynamics. Here, in this study, we use this extended landscape method for

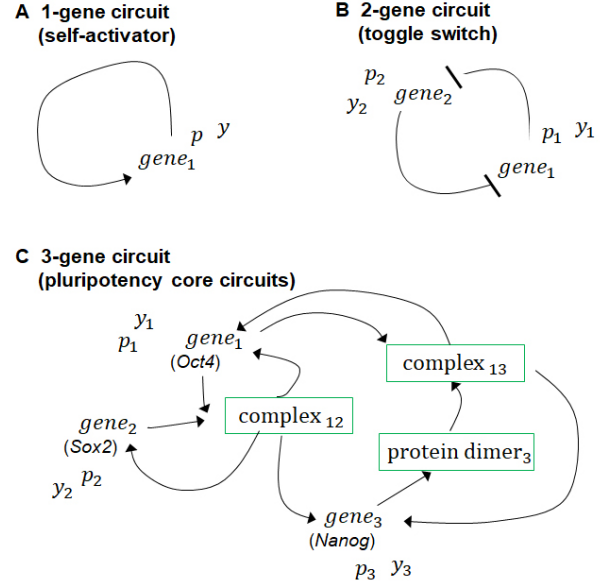


FIG. 3. Gene circuits examined in this study: (*Circuit A*) A self-activating single-gene circuit, (*Circuit B*) a mutually repressing two-gene circuit, and (*Circuit C*) a circuit modeling interactions among three core genes, *Oct4*, *Sox2*, and *Nanog*, which maintain pluripotency in mouse embryonic stem (mES) cells. Lines ending with arrowheads represent activating regulation, and lines ending with bars represent repressive regulation.

generic circuits consisting of multiple genes, leading to

$$\begin{aligned} \frac{1}{k} \frac{dp_i}{dt} &= G_{p_i} - F_{p_i} + \eta_{p_i}, \\ \frac{1}{\omega_i k} \frac{dy_i}{dt} &= G_{y_i} - F_{y_i} + \eta_{y_i}, \end{aligned} \quad (4)$$

where ω_i , which is defined by Eq. 2, is the adiabaticity parameter that measures the ratio of the rate to change y_i over the rate to change p_i at the i th gene. In Eq. 4, G_{p_i} , G_{y_i} , F_{p_i} , and F_{y_i} are

$$\begin{aligned} G_{p_i} &= (\xi_{11} y_{i+}^2 + 2\xi_{10} y_{i+} y_{i-} + \xi_{1-1} y_{i-}^2) x_i \\ &\quad + (\xi_{01} y_{i+}^2 + 2\xi_{00} y_{i+} y_{i-} + \xi_{0-1} y_{i-}^2) (1 - x_i), \\ G_{y_i} &= [\bar{r}^{0-1} y_{i-}^2 + 2\bar{r}^{10} y_{i+} y_{i-}] / k, \\ F_{p_i} &= p_i, \\ F_{y_i} &= [2\bar{r}^{-10} y_{i+} y_{i-} + \bar{r}^{01} y_{i+}^2] / k, \end{aligned} \quad (5)$$

with $y_{i+} = (1 + y_i)/2$, $y_{i-} = (1 - y_i)/2$, and $\xi_{xy} = g_{xy}/(k\Omega)$, which is the normalized protein-synthesis rate at the chromatin state x and y .

As the saddle-point approximation, i.e., the truncation of fluctuations at the 2nd order, was used in deriving Eq. 4, terms η_{p_i} and η_{y_i} in the r.h.s. of Eq. 4 represent Gaussian random noises, satisfying $\langle \eta_{p_i}(t) \rangle = \langle \eta_{y_i}(t) \rangle = 0$, $\langle \eta_{p_i}(t) \eta_{p_j}(t') \rangle = 2D_{p_i} \delta_{ij} \delta(t - t')$, and $\langle \eta_{y_i}(t) \eta_{y_j}(t') \rangle = 2D_{y_i} \delta_{ij} \delta(t - t')$ with D_{p_i} and D_{y_i} being

diffusion constants,

$$\begin{aligned} D_{p_i} &= \frac{1}{2\Omega} (G_{p_i} + F_{p_i}), \\ D_{y_i} &= \frac{1}{2\omega_i} (G_{y_i} + F_{y_i}). \end{aligned} \quad (6)$$

From Eq. 6, we see that the volume Ω and the adiabaticity ω determine the fluctuation amplitude of p and y , respectively.

By numerically integrating Eq. 4, we calculate the stationary distribution of $\{p\}$ and $\{y\}$, probability currents, and other quantities. In the following, we regard $1/k$ as units of time by adopting $k = 1$. See Appendix A for details of the numerical calculation.

We apply this model to circuits of interacting genes. Biochemical analysis has shown that the slow histone-state dynamics bring about prominent feedback effects in eukaryotic cells [44]. While this experimental analysis is on the gene circuits involving complex repressive regulations, we use in the present study more idealized circuits to highlight the physical principles of the eddy dynamics effects. We examine the *Circuits A*, *B*, and *C* in Fig. 3. Refer to Appendix B and Table II for the details of each circuit.

III. LANDSCAPES AND NONEQUILIBRIUM FLUCTUATIONS

In this section, we investigate the basic features of the effects of nonadiabaticity by applying the model to *Circuits A* and *B*.

A. Basin distribution in nonadiabatic landscapes

The illustration in Fig. 1 suggests that the basin distribution of the landscape changes as ω varies. We demonstrate that this change indeed takes place in the eddy regime of $0.1 \lesssim \omega \lesssim 1$.

Fig. 4 shows the landscape, $U(p, y) = -\log P(p, y)$, which was obtained from the stationary distribution, $P(p, y)$, in the self-activating single-gene circuit (*Circuit A*). In the large ω case, the landscape has a single basin at the active state of $y \approx 1$. The basin lies parallel to the y -axis, showing a large fluctuation in y but a confined fluctuation in p . As ω decreases, the landscape develops two basins; one at the active state with large y and p , and the other at the inactive state with small y and p . The inactive basin appears at a distant position from the active basin at the mild nonadiabaticity. In the case of parameters used in Fig. 4, the inactive basin appears at $\omega \approx 0.5$. For the smaller $\omega < 0.5$, the landscape extends in both directions of p and y , resulting in large correlated fluctuations in p and y .

Similarly, in the landscape of a mutually repressing two-gene circuit (*Circuit B*), the number of basins increases as the adiabaticity parameter ω decreases.

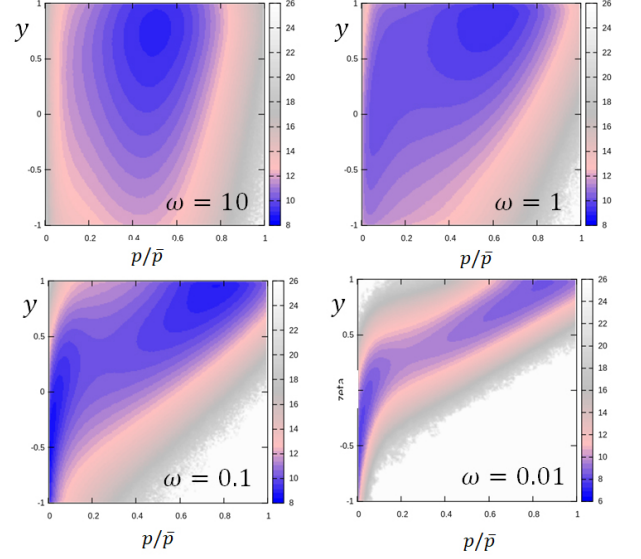


FIG. 4. The landscape, $U(p, y)$, of the self-activating single-gene circuit, *Circuit A*, derived from the numerically obtained distribution of p and y . $\bar{p} = 1.0$.

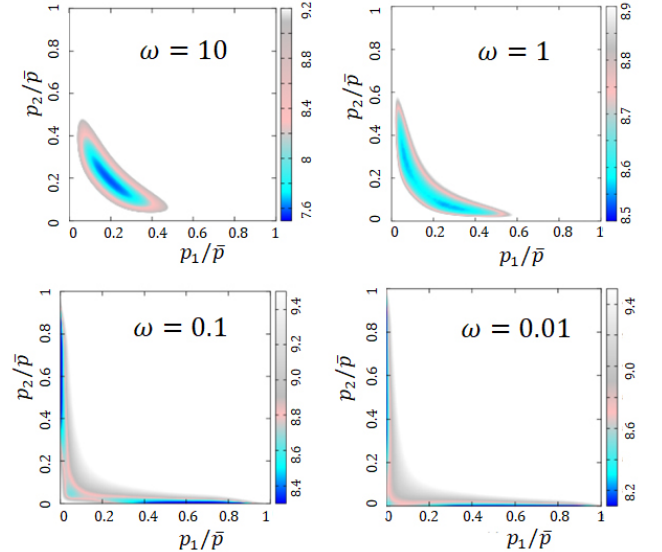


FIG. 5. The landscape, $U(p_1, p_2)$, of the mutually repressing two-gene circuit, *Circuit B*, derived by projecting the numerically obtained distribution of p_1 , p_2 , y_1 , and y_2 onto the two-dimensional plane of p_1 and p_2 . $\bar{p} = 1.2$. Regions of high $U(p_1, p_2)$ values are represented in white.

We numerically calculated the steady-state distribution $P(p_1, p_2, y_1, y_2)$, and plotted the two-dimensional landscape $U(p_1, p_2) = -\log(\iint dy_1 dy_2 P(p_1, p_2, y_1, y_2))$ (Fig. 5). When the typical protein concentration \bar{p} is moderately small ($\bar{p} < 1.5$) and the adiabaticity ω is large, the landscape $U(p_1, p_2)$ has a single basin at the diagonal position, $p_1 = p_2$, on the p_1 - p_2 plane, corre-

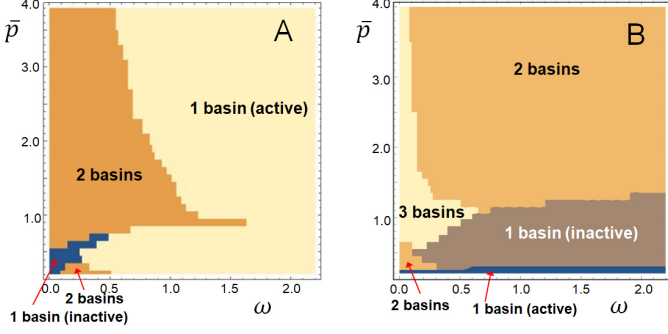


FIG. 6. Phase diagram of the number of basins on the landscape. (A) The number of basins on the landscape, $U(p, y)$, of the self-activating single-gene circuit, *Circuit A*. (B) The number of basins on the landscape, $U(p_1, p_2)$, of the mutually repressing two-gene circuit, *Circuit B*. Phase diagrams were drawn by sampling about 10^3 points on the ω - \bar{p} plane and counting the number of basins on the numerically obtained steady-state distributions. Lines representing the phase boundaries are not smooth due to the finite number of sampled points.

sponding to the inactive state with small p and y . As ω decreases, the basin at the diagonal position bifurcates into two basins at off-diagonal positions, one at $p_1 > p_2$ and $y_1 > y_2$ and the other at $p_1 < p_2$ and $y_1 < y_2$. With further decreases in ω , the two off-diagonal basins deepen, and an additional shallow basin emerges at the diagonal position, representing the inactive state. In this scenario, the two off-diagonal basins dominate the dynamics, causing the system to function as a toggle switch between those two states. When \bar{p} is large ($\bar{p} > 1.5$) in *Circuit B*, the landscape has two basins at off-diagonal positions even with a large ω , and reducing ω generates an extra third basin at the diagonal position of the inactive state. Overall, in both scenarios, the landscape extends over multiple basins when $\omega < 1$, indicating increased fluctuations in p_1 and p_2 .

We summarize the characteristics of basins of *Circuits A* and *B* in phase diagrams of Figs. 6A and 6B, respectively. In both Figs. 6A and 6B, despite the presence of complex phase-diagram structures at $\bar{p} < 1$ due to significant fluctuations in p_i , we notice a consistent trend of increasing basin numbers as the parameter ω decreases, regardless of the \bar{p} value. This rise in basin numbers is observed within the ω range of the eddy regime of $0.1 \lesssim \omega \lesssim 1$. With the increase in basin numbers, the landscape extends across multiple basins, indicating enhanced fluctuations in the expression level.

B. Hysteresis and time-ordering in the eddy regime

The changes in the landscape in the eddy regime should alter fluctuations in p and y . We can analyze this effect by calculating the probability current, $\vec{J} = (\{J_{p_i}\}, \{J_{y_i}\})$, with

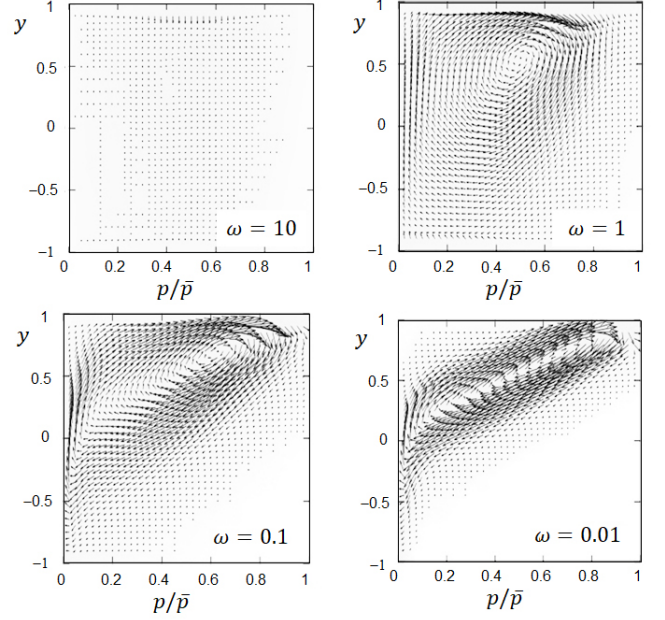


FIG. 7. The probability current $\vec{J}(p, y)$ of the self-activating single-gene circuit, *Circuit A*, is plotted as arrows on the p - y plane. The same parameters used in Fig. 4 were employed.

$$\begin{aligned} J_{p_i} &= (G_{p_i} - F_{p_i}) P(\{p\}, \{y\}) - \frac{\partial}{\partial p_i} [D_{p_i} P(\{p\}, \{y\})], \\ J_{y_i} &= (G_{y_i} - F_{y_i}) P(\{p\}, \{y\}) - \frac{\partial}{\partial y_i} [D_{y_i} P(\{p\}, \{y\})]. \end{aligned} \quad (7)$$

The divergence-free circular flow of \vec{J} in a steady state is a hallmark of broken detailed balance, indicating nonequilibrium dissipation that drives the fluctuation [45–47]. Fig. 7 shows the probability current in the self-activating single-gene circuit (*Circuit A*). When $\omega \gg 1$, the current is not very noticeable in the steady state, suggesting that the state can be effectively approximated by an equilibrium. Conversely, in the nonadiabatic case of $\omega \lesssim 1$, the circular flux of the probability current becomes evident, explicitly breaking the detailed balance. The circular flux spreads globally over the p - y plane in the eddy regime of $0.1 \lesssim \omega \lesssim 1$, but the area showing the intense current becomes narrower in the strongly nonadiabatic case of $\omega \lesssim 0.01$.

In the previous publication [13], the authors demonstrated that the most probable pathways—those that contribute the most weight in the path-integral representation of the transition probability between the active and inactive states of a self-activating single-gene circuit—align with the direction of the circular flux in its extended landscape. Consequently, the pathway generated in one direction differed from the pathway in the reverse direction, indicating the presence of hysteresis.

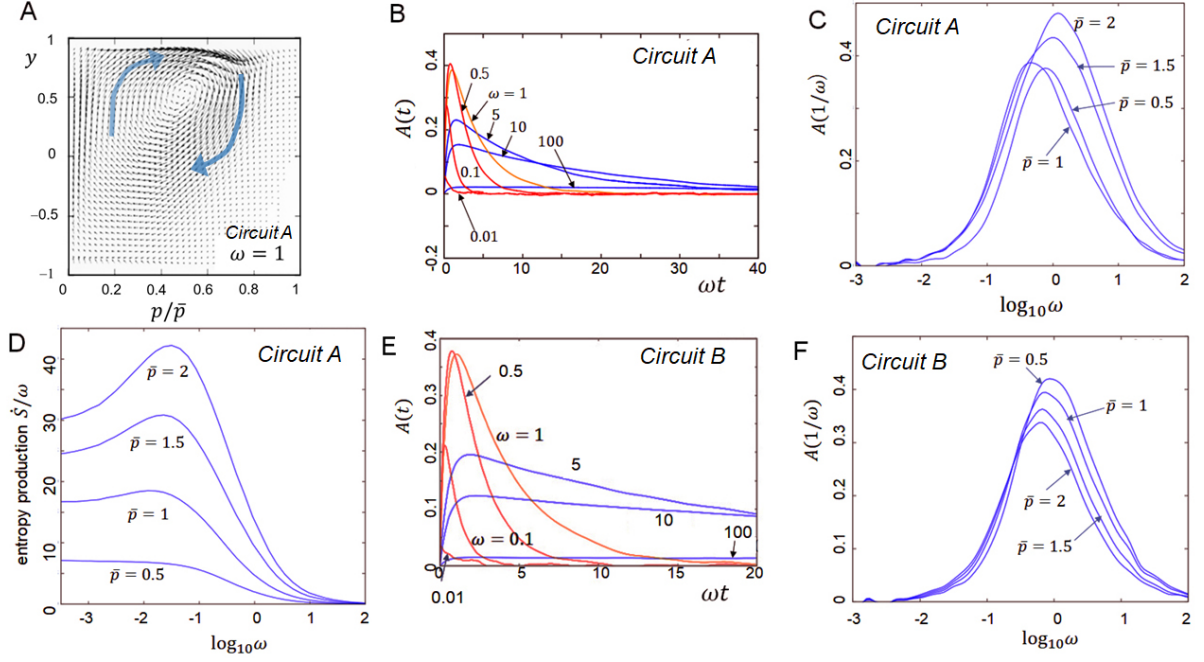


FIG. 8. Prominent nonequilibrium features in the eddy regime of $0.1 \lesssim \omega \lesssim 1$. (A) The circular flux of the probability current leads to hysteresis in the switching dynamics. The same plot as a panel in Fig. 7. (B) The cross-correlation function $A(t)$ in the self-activating single-gene circuit, *Circuit A*, is plotted as a function of t for various values of ω ; $\omega = 1$ (orange), $\omega = 5, 10, 100$ (blue), and $\omega = 0.5, 0.1, 0.01$ (red). (C) The value of the cross-correlation $A(t = 1/\omega)$ in *Circuit A* is plotted as a function of ω for various values of \bar{p} . (D) Entropy production during the typical chromatin-state turnover time, \dot{S}/ω , in *Circuit A* is plotted as a function of ω for various values of \bar{p} . (E) The cross-correlation function $A(t)$ in the mutually repressing two-gene circuit, *Circuit B*, is plotted as a function of t for various values of ω ; $\omega = 1$ (orange), $\omega = 5, 10, 100$ (blue), and $\omega = 0.5, 0.1, 0.01$ (red). (F) The value of the cross-correlation function $A(t = 1/\omega)$ in *Circuit B* is plotted as a function of ω for various values of \bar{p} .

Similarly, when following the direction of the globally developed circular flux in Fig. 7, we observe that the transition from the inactive state to the active state and the reverse transition should follow distinct pathways. Therefore, we expect that the global circular flux within the range of $0.1 \lesssim \omega \lesssim 1$ (Fig. 7 and Fig. 8A) in the present system indicates that the transition between the two states exhibits hysteresis. This expectation is confirmed through the calculation of the cross-correlation function.

$$A(t) = \frac{\langle (\delta y(\tau) \delta p(\tau + t) - \delta y(\tau + t) \delta p(\tau)) \rangle_\tau}{\Delta y \Delta p}, \quad (8)$$

where $\langle \dots \rangle_\tau$ represents the average over τ , $\delta y(t) = y(t) - \langle y(t_0) \rangle_{t_0}$, and $\delta p(t) = p(t) - \langle p(t_0) \rangle_{t_0}$. Δy and Δp are defined by $\Delta y = \langle \delta y(\tau)^2 \rangle_\tau^{1/2}$ and $\Delta p = \langle \delta p(\tau)^2 \rangle_\tau^{1/2}$. If there is a tendency for time-ordered changes with variation in y preceding the p variation, then $A(t) > 0$ for $t > 0$. The calculated results in Fig. 8B indeed show $A(t) > 0$ for $t > 0$, confirming the tendency that the chromatin state y changes first and the product-protein concentration p follows in both transitions from inactive to active and from active to inactive states, resulting in

different pathways with hysteresis. $A(t)$ shows a peak at the typical turnover time of the chromatin state change, $t \approx 1/\omega$.

In Fig. 8C, $A(1/\omega)$ is plotted as a function of ω , showing that the tendency for cross-correlation, or time-ordering, is most pronounced in the eddy regime of $0.1 \lesssim \omega \lesssim 1$. In contrast, this tendency weakens in the strongly adiabatic regime ($\omega \gg 1$). This observation aligns with the results presented in Fig. 7, where the circular flux develops significantly in the eddy regime but diminishes in the strongly adiabatic regime. In the strongly nonadiabatic regime ($\omega \ll 1$), the cross-correlation $A(1/\omega)$ is also weaker because the probability current becomes confined to a localized area, although the intensity of the current remains high within that area. The narrower distribution of current shown in Fig. 7 for $\omega = 0.01$ suggests that changes in protein concentration tend to closely follow changes in histone states. This leads to both active-to-inactive and inactive-to-active pathways approaching a line that connects two basins. The convergence of these pathways should reduce hysteresis, resulting in a smaller value of $A(1/\omega)$.

The amount of non-equilibrium dissipation can be measured by calculating the entropy production rate,

$$\dot{S} = \iint dp ds \left(\frac{J_p(p, v)^2}{P(p, v)D_p} + \frac{J_v(p, v)^2}{P(p, v)D_v} \right). \quad (9)$$

In Fig. 8D, entropy \dot{S}/ω produced during the chromatin-state turn-over time $1/\omega$ is plotted. Fig. 8D shows that entropy production \dot{S}/ω remains low in the adiabatic regime of $\omega > 1$, approaching 0 in the adiabatic limit as $\omega \gg 1$. This observation is in line with the finding that the circular flux disappears in the adiabatic limit. As ω becomes smaller, the nonequilibrium dissipation indicated by \dot{S}/ω begins to rise in the eddy regime of the range $0.1 \lesssim \omega \lesssim 1$. This rise in nonequilibrium dissipation corresponds to a shift in landscape structure, where the circular flux leads to time-ordering tendencies and hysteresis.

While the cross-correlation $A(1/\omega)$ shows a peak in the eddy regime of $0.1 \lesssim \omega \lesssim 1$, entropy production \dot{S}/ω continues to increase in this regime as ω decreases further. This rise is attributed to the increasing intensity of the probability current in the nonadiabatic regime. While $A(t)$ reflects the global pattern of circular flux and diminishes as the current becomes confined to a narrow area (as in the case of $\omega = 0.01$ in Fig. 7), entropy production \dot{S}/ω reflects the intensity of that current and increases as the intensity grows with further decreases in ω . Interestingly, \dot{S}/ω exhibits a peak in the intensely nonadiabatic regime of $0.01 \lesssim \omega \lesssim 0.1$ and tends to decrease as ω further decreases, suggesting that the current confined to a narrow area (narrower than shown in Fig. 7) begins to contribute less to the overall dissipation.

The time-ordering tendency and hysteresis are also observed in the mutually repressing two-gene circuit (*Circuit B*). The cross-correlation, $A(t)$ of Eq. 8, is plotted in Fig. 8E using $\delta y(t) = y_1(t) - y_2(t)$, $\delta p(t) = p_1(t) - p_2(t)$, showing $A(t) > 0$ for $t > 0$. $A(1/\omega)$ is plotted in Fig. 8F, demonstrating that the cross-correlation is most prominent in the eddy regime.

Taken together, the examples of single-gene (*Circuit A*) and two-gene (*Circuit B*) circuits illustrate that the landscape exhibits different structures in the adiabatic and nonadiabatic limits with the increased number of basins in the nonadiabatic limit. In the transitional or eddy regime between these limits, fluctuations grow as the probability current shows a well-developed circular flow, which is associated with significant entropy production. This established circular flow results in hysteresis in gene-switching dynamics, leading to a temporal ordering of processes, where the slow change in chromatin state occurs before the fast change in transcription activity.

IV. FLUCTUATIONS IN THE THREE-GENE MODEL

A. The large Nanog fluctuation in mES cells

The three core genes, *Oct4*, *Sox2*, and *Nanog*, activate each other and regulate many other genes in mES cells, playing essential roles in maintaining pluripotency [48–50]. Here, we write the gene's name in *italic* and the protein's name in roman. These genes remain active when cells are cultivated in a medium containing 2i factors [51]. Without 2i, cells still maintain pluripotency when cultivated with Lif, but they show a significant fluctuation in Nanog concentration from cell to cell [52–54]. These cells show transitions between high and low-Nanog cell states during several cell cycles [53]. As losing Nanog is a trigger to differentiation [55], the large Nanog fluctuation is the fluctuation of cells at the doorway to differentiation. However, in the same population of cells, Oct4 and Sox2 do not fluctuate intensely and instead show narrow single-peak distributions of their concentrations [53].

Models of the gene network were proposed to explain the difference in activity fluctuation among the three core genes [25, 53, 56, 57]. A typical assumption used in the models was the self-activating interaction of *Nanog* [56] and the repressing interactions between *Nanog* and other genes [53, 56]. These assumptions allowed the models to explain the switching fluctuation between active and inactive states in *Nanog* and the lack of relevance of other genes to this fluctuation. However, the self-repression of *Nanog* was reported [58] and the mutual repression among these genes seem to play a minor role [50]; therefore, further careful consideration on the gene-circuit structure is necessary to analyze the heterogeneous fluctuations in these genes. In this study, we use our model of chromatin-state transitions to analyze this problem without assuming the mutual repression among these three genes.

B. Large fluctuations in the three-gene model

We investigated a gene circuit composed of the three core genes in mES cells (*Circuit C*). In this circuit, unlike the previous models [53, 56], a direct self-activation of *Nanog* is not considered, but the mutual activation of three genes, *Oct4*, *Sox2*, and *Nanog*, through the observed complex formation of TFs [23, 48, 50, 59, 60] is assumed. This gene circuit behaves similarly to *Circuit A*, showing a similar dependence on the adiabaticity parameter ω . We calculated a two-dimensional landscape $U(p_1, p_3)$ based on the projected distribution $P(p_1, p_3)$, where p_1 represents the concentration of Oct4 and p_3 represents the concentration of Nanog. In Fig. 9, we show $U(p_1, p_3)$ for various values of $\omega = \omega_1 = \omega_2 = \omega_3$. Additionally, Fig. 9 shows the projection of the cubic landscape $U(p_1, p_2, p_3)$ onto the two-dimensional plane to demonstrate the basin distribution in the three-

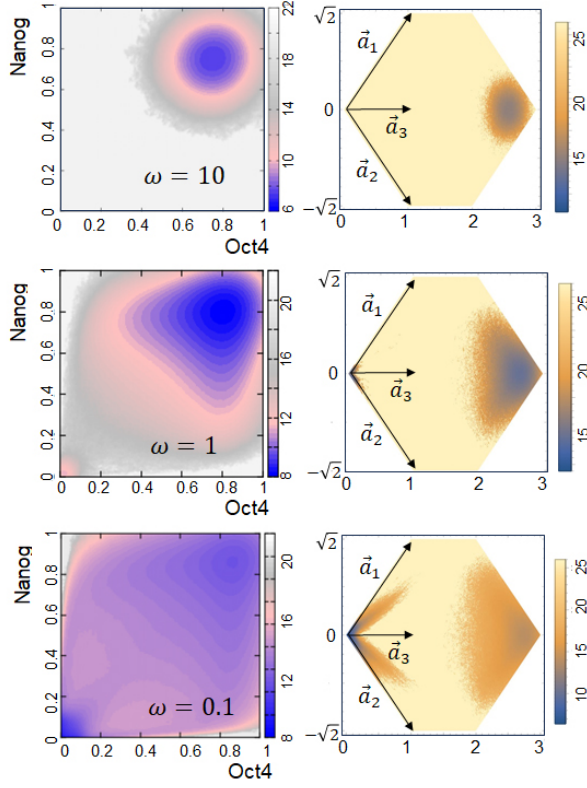


FIG. 9. The landscape of the circuit of the three core genes of mES cells, *Circuit C*, calculated with various values of the adiabaticity parameter $\omega = \omega_1 = \omega_2 = \omega_3$. The typical concentrations were set to $\bar{p}_1 = \bar{p}_2 = \bar{p}_3 = 2$. (Left) The two-dimensional landscape $U(p_1, p_3)$ plotted on the plane of p_1/\bar{p}_1 (normalized Oct4 concentration) and p_3/\bar{p}_3 (normalized Nanog concentration). (Right) The three-dimensional landscape $U(p_1, p_2, p_3)$, with p_2 being the Sox2 concentration, projected on the two-dimensional plane using the coordinate $(p_1/\bar{p}_1)\vec{a}_1 + (p_2/\bar{p}_2)\vec{a}_2 + (p_3/\bar{p}_3)\vec{a}_3$ with $\vec{a}_1 = (1, \sqrt{2})$, $\vec{a}_2 = (1, -\sqrt{2})$, and $\vec{a}_3 = (1, 0)$.

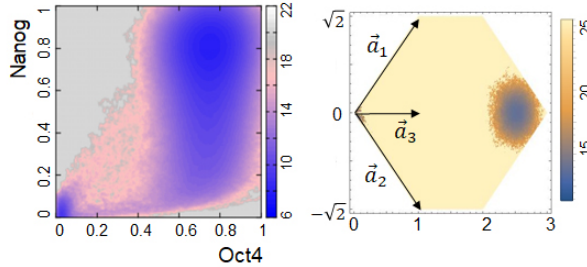


FIG. 10. The landscape of the circuit of the three core genes of mES cells, *Circuit C*, calculated with the heterogeneous adiabaticity parameters, $\omega_1 = \omega_2 = 10$ for Oct4 and Sox2 and $\omega_3 = 0.5$ for Nanog. Other parameters are the same as in Fig. 9. (Left) The two-dimensional landscape $U(p_1, p_3)$. (Right) The three-dimensional landscape $U(p_1, p_2, p_3)$. The ways of plotting landscapes are the same as in Fig. 9.

dimensional space, with p_2 representing the concentration of Sox2.

When ω is large, the landscape has a single basin at the active state, and when ω is small, it has two basins at the active and inactive states. At a large value of $\omega = 10$, the active basin restricts fluctuations to a narrow region, while at a small value of $\omega = 0.1$, the landscape extends globally over the active and inactive basins, allowing large fluctuations in p_1 , p_2 , and p_3 . Since ω controls the fluctuation amplitude, we can propose a mechanism of using the heterogeneous ω_i to explain the experimentally observed heterogeneous fluctuations among the three core genes. It is expected that ω_3 of *Nanog* is small, like generic eukaryotic genes, allowing the large fluctuation, but we assume that ω_1 of *Oct4* and ω_2 of *Sox2* are larger for unknown reason, suppressing fluctuations. However, as explained below, this mechanism does not explain the experimentally observed small fluctuations in Oct4 and Sox2.

Fig. 10 shows the calculated landscape with heterogeneous adiabaticity parameters: $\omega_1 = \omega_2 = 10$ and $\omega_3 = 0.5$. Due to the activating interactions among three genes, a small ω value for one gene was enough to create an inactive basin shared by all three genes. This led to an extended landscape that allows for large fluctuations with bimodal distributions of p_1 , p_2 , and p_3 . This does not explain the experimentally observed single-peak distribution of p_1 (Oct4) and p_2 (Sox2). While further calibration of the parameters could potentially lead to the single-peak distributions, the model still generated bimodal distributions of p_1 and p_2 as long as moderate values for the activating interactions among the three genes were assumed in our parameter choices. Therefore, the mechanism of heterogeneous ω_i in *Circuit C* does not provide a straightforward explanation for the experimentally observed heterogeneous fluctuations in protein concentration.

V. DEEP EPIGENETIC REGULATION

To address the issue of heterogeneous fluctuations in mES cells, we propose a model that introduces an additional degree of freedom to describe chromatin condensation. In the model discussed in Section IV, we assumed that the histone state within the chromatin domain directly influences the degree of condensation of that domain. Although there is a correlation between the properties of the domain and histone states, it is not perfect; other proteins and RNAs also play a role in affecting domain characteristics. Specifically, observed transcriptional bursting indicates that the transcription initiation complex—a complex of TFs, mediators, coactivators, RNA polymerase, and other molecules—is formed and resolved near the enhancer and promoter over a timescale of $10^2 \sim 10^3$ s. This process is associated with changes in the structure of the chromatin region involving the enhancer and promoter, even while the domain-wide

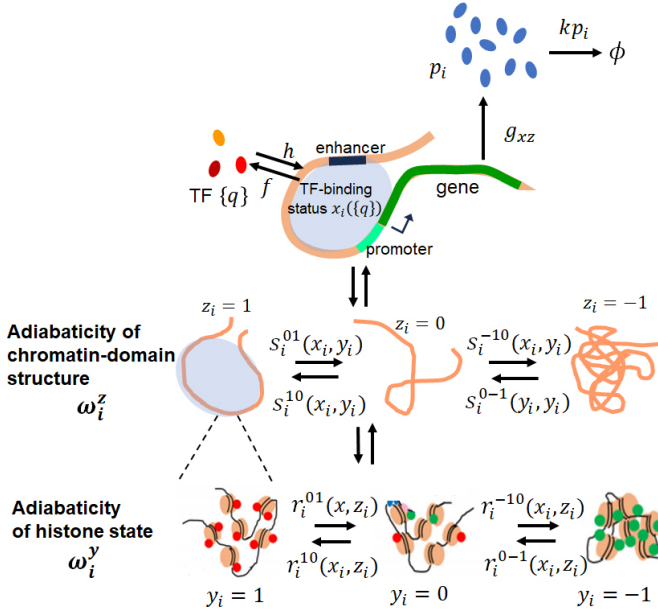


FIG. 11. Deep Epigenetic Regulation. In addition to the scheme shown in Fig. 2, we represent the chromatin domain structure of the i th gene with the following notations: $z_i = -1$ indicates that the chromatin domain to which the i th gene belongs is of inactive type, $z_i = 0$ indicates that the domain is of active type, and $z_i = 1$ indicates that the domain is of active type and forms a transcription initiation complex. The protein synthesis rate, denoted as g_{xz} , depends on the transcription factor-binding status x_i as well as the chromatin domain structure z_i . The value of z_i can change through transitions occurring at a rate $s_i^{zz'}$, which depends on x_i and the histone state y_i . Additionally, the histone state transition rate, $r_i^{yy'}$, depends on both x_i and z_i . This multi-layered regulation within the chromatin is referred to as deep epigenetic regulation.

histone state remains fixed [31–33]. To capture these fluctuations in chromatin structure, we introduce a variable z_i , which represents the domain structure of the i th gene. We define $z_i = -1$ when the domain of the i th gene is condensed, $z_i = 0$ when the domain has a region of an extended structure near the enhancer and promoter, and $z_i = 1$ when the extended region of the domain forms a transcription initiation complex. Refer to Fig. 11 for a schematic representation of the model.

We consider that the protein-synthesis rate, $g(x_i, z_i)$, depends explicitly on the TF-binding status x_i and the chromatin-domain structure z_i , and indirectly on the histone state y_i through the dependence of z_i on y_i . We define the transition rates $s_i^{zz'}$ and $r_i^{yy'}$ at the domain containing the i th gene; transitions from the chromatin-domain structure z_i' to z_i occur at the rate $s_i^{zz'}$, and transitions from the histone-state y_i' to y_i occur at the rate $r_i^{yy'}$. We define parameters $\bar{s}^{zz'}$ and $\bar{r}^{yy'}$, which are of order of k , characterizing the transitions. Then, we introduce two adiabaticity parameters, the chromatin-structure adiabaticity ω_i^z and the histone-state adiabatic-

ity ω_i^y , and write

$$\begin{aligned} s_i^{zz'} &= \omega_i^z \bar{s}^{zz'}, \\ r_i^{yy'} &= \omega_i^y \bar{r}^{yy'}. \end{aligned} \quad (10)$$

The parameters ω_i^z and ω_i^y measure the ratios of rates of z and y transitions over the rate of the p fluctuation at the i th gene; Eq. 10 shows $s_i^{zz'} = O(\omega_i^z k)$ and $r_i^{yy'} = O(\omega_i^y k)$.

Chromatin structure should be changed by the TF binding and the histone modification, and the binding rate of the histone modifier enzymes should depend on the TF binding and the chromatin structure [35, 61, 62]. These relationships should lead to the expression that the chromatin-structure transition rate $s_i^{zz'}$ and its normalized value are functions of x_i and the histone state y_i as $s_i^{zz'}(x_i, y_i)$ and $\bar{s}^{zz'}(x_i, y_i)$, and the histone-state transition rate $r_i^{yy'}$ and its normalized value are functions of the TF state x_i and the chromatin-domain structure z_i as $r_i^{yy'}(x_i, z_i)$ and $\bar{r}^{yy'}(x_i, z_i)$. We use the first-order approximation and write;

$$\bar{s}^{zz'}(x_i, y_i) = \nu^{zz'} + \sigma_x^{zz'} x_i + \sigma_y^{zz'} y_i, \quad (11)$$

$$\bar{r}^{yy'}(x_i, z_i) = \mu^{yy'} + \gamma_x^{yy'} x_i + \gamma_z^{yy'} z_i, \quad (12)$$

with $z_{i+} = (1 + z_i)/2$. Here, $\nu^{zz'}$, $\sigma_x^{zz'}$, $\sigma_y^{zz'}$, $\mu^{yy'}$, $\gamma_x^{yy'}$, and $\gamma_z^{yy'}$ are the coefficients of the order of k . Thus, we have a multilayer regulation mechanism through physical transitions of z and chemical transitions of y in chromatin. We expect that the increased degrees of freedom afforded by this multilayer regulation allow for flexible tuning of circuit performance, and we call this multilayer regulation *deep epigenetic regulation* or *deep epigenetics*.

Biochemical analyses, including studies on the complex cross-talks among histone modifier enzymes, have highlighted the relationships between chromatin structure, TF binding, and histone modifications [35, 61, 62]. Although a comprehensive physical model of these relationships has not yet been established, we assume that changes in these states are consistent with one another. Specifically, an activating or repressive histone state is expected to correlate with an open or condensed chromatin structure near the enhancer and promoter within the domain. Moreover, an open or condensed chromatin structure is anticipated to recruit activating or repressive histone-modifier enzymes. This consistency can be summarized as $\sigma_y^{-10} \approx \sigma_y^{01} < 0$, $\sigma_y^{10} \approx \sigma_y^{0-1} > 0$, $\gamma_z^{-10} \approx \gamma_z^{01} < 0$, and $\gamma_z^{10} \approx \gamma_z^{0-1} > 0$. In the current model, we consider only the mutual activation among three genes; therefore, the transitions toward inactive states are $\sigma_x^{01} \approx \sigma_x^{-10} < 0$ and $\gamma_x^{01} \approx \gamma_x^{-10} < 0$, and the transitions toward active states are $\sigma_x^{10} \approx \sigma_x^{0-1} > 0$ and $\gamma_x^{10} \approx \gamma_x^{0-1} > 0$. Values of these coefficients used in the current study are summarized in Table III.

In the deep epigenetic regulation model, Eq. 4 with $k =$

1 is replaced by

$$\begin{aligned}\frac{dp_i}{dt} &= G_{p_i} - F_{p_i} + \eta_{p_i}, \\ \frac{1}{\omega_i^z} \frac{dz_i}{dt} &= G_{z_i} - F_{z_i} + \eta_{z_i}, \\ \frac{1}{\omega_i^y} \frac{dv_i}{dt} &= G_{y_i} - F_{y_i} + \eta_{y_i},\end{aligned}\quad (13)$$

with $\langle \eta_{z_i}(t) \rangle = \langle \eta_{p_i}(t) \eta_{z_j}(t') \rangle = \langle \eta_{y_i}(t) \eta_{z_j}(t') \rangle = 0$, and $\langle \eta_{z_i}(t) \eta_{z_j}(t') \rangle = 2D_{z_i} \delta_{ij} \delta(t - t')$, and Eq. 6 becomes

$$\begin{aligned}D_{p_i} &= \frac{1}{2\Omega} (G_{p_i} + F_{p_i}), \\ D_{z_i} &= \frac{1}{2\omega_i^z} (G_{z_i} + F_{z_i}), \\ D_{y_i} &= \frac{1}{2\omega_i^y} (G_{y_i} + F_{y_i}).\end{aligned}\quad (14)$$

In Eq. 13, by writing $\xi(x, z) = g(x, z)/(k\Omega)$, $z_{i+} = (1 + z_i)/2$, and $z_{i-} = (1 - z_i)/2$, we have

$$\begin{aligned}G_{p_i} &= (\xi(1, 1)z_{i+}^2 + 2\xi(1, 0)z_{i+}z_{i-} + \xi(1, -1)z_{i-}^2)x_i \\ &\quad + (\xi(0, 1)z_{i+}^2 + 2\xi(0, 0)z_{i+}z_{i-} + \xi(0, -1)z_{i-}^2)(1 - x_i), \\ G_{z_i} &= \bar{s}^{0-1}z_{i-}^2 + 2\bar{s}^{10}z_{i+}z_{i-}, \\ G_{y_i} &= \bar{r}^{0-1}y_{i-}^2 + 2\bar{r}^{10}y_{i+}y_{i-}, \\ F_{p_i} &= p_i, \\ F_{z_i} &= 2\bar{s}^{-10}z_{ia}z_{i-} + \bar{s}^{01}z_{i+}^2, \\ F_{y_i} &= 2\bar{r}^{-10}y_{i+}y_{i-} + \bar{r}^{01}y_{i+}^2.\end{aligned}\quad (15)$$

We apply this model to *Circuit C* by representing the chromatin-domain structure around *Oct4*, *Sox2*, and *Nanog* as z_1 , z_2 , and z_3 , respectively. The histone-state transitions are assumed to occur over several cell cycles [21, 22], with small histone-state adiabaticity as $\omega_1^y = \omega_2^y = \omega_3^y = 0.1$. We assume that the chromatin structure around *Oct4* and *Sox2* fluctuates in a similar timescale to transcriptional bursting transitions $10^2 \sim 10^3$ s, which implies the chromatin-structure adiabaticity $\omega_i^z = 10 \sim 100$. In the current study, we use $\omega_1^z = 10$ and $\omega_2^z = 10$ for *Oct4* and *Sox2*, respectively.

As cells start differentiation, the chromatin structure around the three core genes, *Oct4*, *Sox2*, and *Nanog*, are reorganized [63, 64]. Domains containing the three core genes, *Oct4*, *Sox2*, and *Nanog*, are part of the μ m-size structure, the active compartment (compartment A), in mES cells, but they switch to the inactive compartment (compartment B) upon inactivation through differentiation. In particular, the compartment switching of *Nanog* takes place just after initiation of differentiation [65, 66], suggesting that the large-scale conformation fluctuation of the domain containing *Nanog* occurs in mES cells as a precursor fluctuation. Therefore, we assume that *Nanog* shows a large-scale fluctuation, exhibiting the A/B compartment switching at a period of relatively short cycle of mES cells of $\sim 10^4$ s, resulting in the use of

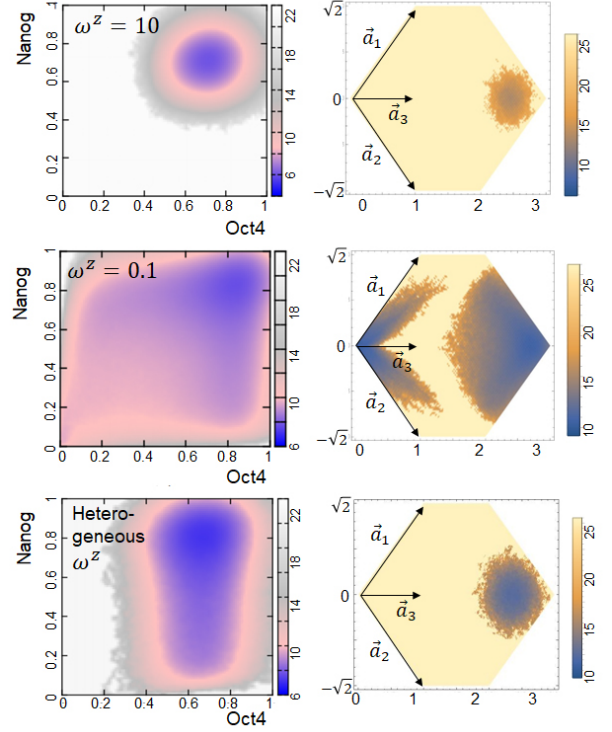


FIG. 12. The landscapes of the circuit of the three core genes of mES cells, *Circuit C*, calculated with the deep epigenetics hypothesis. (Left) The two-dimensional landscape $U(p_1, p_3)$ plotted on the plane of the Oct4 concentration p_1 and the Nanog concentration p_3 . (Right) The three-dimensional landscape $U(p_1, p_2, p_3)$ with p_2 being the Sox2 concentration. (Top and Middle) Calculated with the homogeneous chromatin-structure adiabaticity parameters set as $\omega^z = \omega_1^z = \omega_2^z = \omega_3^z$. (Bottom) Calculated with the heterogeneous chromatin-structure adiabaticity, utilizing a small value for *Nanog*: $\omega_1^z = \omega_2^z = 10$ and $\omega_3^z = 0.5$. The typical concentrations were set to $\bar{p}_1 = \bar{p}_2 = \bar{p}_3 = 2$. Please refer to Table III for other parameters. The ways of plotting landscapes are the same as in Fig. 9 and Fig. 10.

the chromatin-structure adiabaticity $\omega_3^z \approx 0.1 \sim 0.5$ for *Nanog*.

The calculated landscapes in the deep epigenetic regulation model are shown in Fig. 12. The landscape has a single active basin with $\omega_1^z = \omega_2^z = \omega_3^z = 10$, but presents active and inactive basins at $\omega_1^z = \omega_2^z = \omega_3^z = 0.1$. With heterogeneous adiabaticity parameters of $\omega_1^z = \omega_2^z = 10$ and $\omega_3^z = 0.5$ as suggested above, the landscape does not have a definite inactive basin. However, the distribution of the Nanog concentration p_3 is wide, indicating significant fluctuation in the *Nanog* expression, while the distribution of *Oct4* and *Sox2* expression levels is narrow with single-peak distributions. This is consistent with the experimentally observed heterogeneous fluctuations of genes in mES cells.

Thus, the deep epigenetic regulation allows the flexible tuning of fluctuations of individual genes in the circuit,

providing a perspective to analyze how multiple degrees of freedom of the chromatin state are regulated in cells.

VI. DISCUSSION

We studied models of gene circuits made up of one to three interacting eukaryotic genes. We described the speed of changes in the chromatin state using the adiabaticity parameter ω , and investigated the stochastic behaviors of the model by varying ω using the landscape picture. The landscape has different basin structures in the adiabatic ($\omega \gg 1$) and nonadiabatic ($\omega \ll 1$) limits, and it shows enhanced circular flow of the probability current and entropy production in between the two limits, known as the eddy regime ($0.1 \lesssim \omega \lesssim 1$).

The circular flow over the extended landscape, which encompasses both changes in chromatin states and alterations in protein concentration, indicates the presence of hysteresis during transitions between active and inactive state basins. This observation suggests a temporal sequence in which chromatin-state changes precede changes in expression levels. This time ordering was indeed noted during the differentiation process of mouse embryonic cells [67]. While the traditional biochemical perspective may focus on specific proteins or genes that regulate this timing, our model proposes that the time ordering results not from specific regulatory factors in cells, but rather from the interaction between slow and fast processes in gene regulation. In this framework, the slow process governs the system's state transitions, while the fast process reacts to it. This concept, where the slow process determines the system's fate, is similar to findings from simulations of a multilayer network model [1]. The mechanism proposed in this study can be validated if the

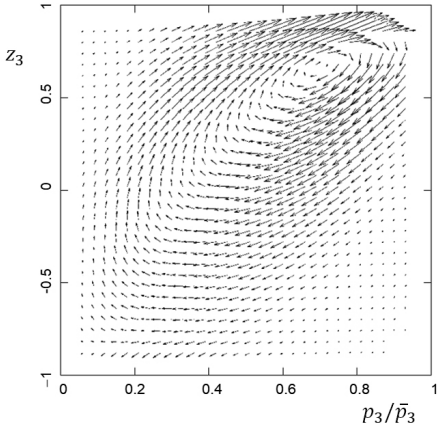


FIG. 13. The probability current $\vec{J} = (J_{p_3}, J_{z_3})$ of the deep epigenetics model of the circuit of three core genes of mES cells, *Circuit C*, projected on the two-dimensional plane of the Nanog concentration p_3 and the chromatin-domain structure z_3 around *Nanog*. The parameters are the same as in the bottom panel of Fig. 12.

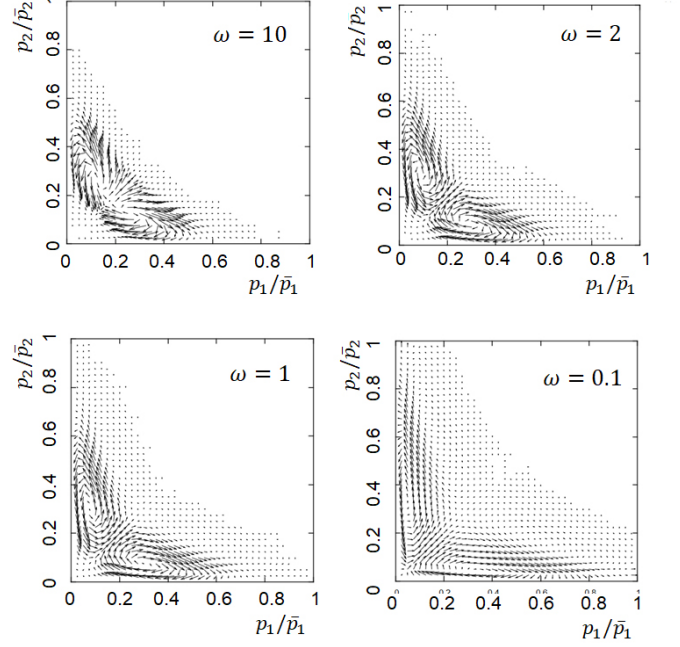


FIG. 14. The probability current $\vec{J} = (J_{p_1}, J_{p_2})$ of the mutually repressing two-gene circuit, *Circuit B*, projected on the two-dimensional p_1 - p_2 plane. The parameters are the same as in Fig. 5.

adiabaticity parameter ω can be controlled in cells. The circular flux is also found in the deep epigenetic regulation model (Fig. 13), suggesting time-ordering tendency and hysteresis in fluctuations of *Nanog* in mES cells. It is interesting to examine this prediction by measuring dynamic fluctuations of mES cells.

Another feature of the circular flux is found in the example of the mutually repressing two-gene circuit (*Circuit B*). This circuit shows a bifurcation of a basin at the diagonal position to a pair of basins at off-diagonal positions in the eddy regime. This bifurcation takes place at $\omega = \omega_c \approx 1.2$ with parameters used in Fig. 5. Fig. 14 shows the probability current plotted on the p_1 - p_2 plane, showing the existence of a pair of circular fluxes rotating in opposite directions around positions of a pair of off-diagonal basins. We find that a pair of fluxes appear even in the case of $\omega > \omega_c$, showing that circular fluxes are a precursor, or a warning sign [68], of the bifurcation. It is intriguing to check this prediction by the RNA-velocity measurement in cells undergoing the switching fluctuations.

Eukaryotic genes are regulated by multiple redundant processes within cells, including DNA methylation, various histone modifications, and the organization of chromatin at various spatial scales. The presence of these redundant regulatory mechanisms raises the question: why do they coexist in chromatin? The deep epigenetic regulation model offers an explanation, suggesting that these interrelated processes work together to flexibly tune fluc-

tuations in the activity of individual genes.

A crucial area for future research is to conduct more direct comparisons of the simulation with experimental data. By employing combined high-throughput methodologies such as Hi-C, ChIP-seq, and RNA-seq, it is becoming possible to infer the landscapes and probability currents of gene regulation in cells [69–72]. Building landscapes and analyzing probability currents from experiments will enable comparisons with the theoretical methods, paving the way for further exploration into the biological physics of gene regulation.

ACKNOWLEDGEMENTS

This work was supported by JSPS-KAKENHI Grants 22H00406 and 24H00061.

APPENDIX

A: Numerical simulations

Eq. 4 and Eq. 13 were numerically solved by the Euler discretization with a time step of $\delta t = 0.01$ for $\omega < 0.5$, $\delta t = 0.001$ for $0.5 \leq \omega < 10$, and $\delta t = 0.0001$ for $10 \leq \omega$. In the discretized calculation, occasional large noise values in Eq. 4 and Eq. 13 caused rare jumps, taking the trajectory out of the physically plausible ranges of $0 \leq p_i$, $-1 \leq y_i \leq 1$, and $-1 \leq z_i \leq 1$. To address this issue, solid walls were assumed at the boundaries of these ranges in the numerical calculations. The area near these boundary walls (5% of the total area) was excluded in the integration in Eq. 9 to prevent the artifact contribution of the reflecting probability flow from the walls.

B: Circuits

Circuit A, Self-activating single-gene circuit

The simplest circuit is a loop involving a single gene that produces a TF which activates itself (Fig. 3A). The self-activation is ubiquitous in cells [73], and this circuit is the same as analyzed in the previous report [13]. In the present study, we investigate this circuit in greater depth and compare the dynamics with entropy production and time asymmetry in cross-correlation, which measures how far the system is from equilibrium.

We assume that the protein dimerizes to become a TF, and this dimerization occurs rapidly enough compared to the rate k that we can express the TF concentration q as

$q \propto p^2$. Then, we write $h = h_0 p^2$ with a constant $h_0 > 0$. We use the adiabatic approximation for representing the TF-binding state x with its equilibrium value $x = h_0 p^2 / (h_0 p^2 + f)$. We write $\bar{p} = \xi_{11}$, which is a typical value of p .

Circuit B, Mutually repressing two-gene circuit

We consider a circuit of mutually repressing two genes (Fig. 3B). Though this mutually repressing circuit is ubiquitous in eukaryotic cells, including the synthetically designed circuit [74], we here consider a simplified model to focus on eddy dynamics of this type of circuit by explicitly analyzing the dynamics of the histone-state variables y_1 and y_2 in genes 1 and 2, respectively.

To highlight the effects of eddy dynamics of the circuit, we assume that two genes have the same parameters; the adiabaticity is measured by the adiabaticity parameter $\omega = \omega_1 = \omega_2$. We consider the case where dimers of protein produced from genes 1 and 2 become TFs binding on genes 2 and 1, respectively, so that $q_1 \propto p_1^2$ and $q_2 \propto p_2^2$, leading to $h^{12} = h_0 p_2^2$ and $h^{21} = h_0 p_1^2$. We use the adiabatic approximation to derive x_1 and x_2 , resulting in $x_1 = x^{12} = h_0 p_2^2 / (h_0 p_2^2 + f)$ and $x_2 = x^{21} = h_0 p_1^2 / (h_0 p_1^2 + f)$. We write $\bar{p} = \xi_{10}$.

Circuit C, Three-gene circuit model of pluripotency

By exploring *Circuits A* and *B*, we analyze how the landscapes and nonequilibrium fluctuations depend on the adiabaticity ω_i of the histone-state dynamics. As an example biological system to apply these concepts of landscapes and nonequilibrium fluctuations, we consider the gene circuit to maintain pluripotency in mES cells composed of mutually activating three genes, *Oct4* ($i = 1$), *Sox2* ($i = 2$), and *Nanog* ($i = 3$) [49, 50] (Fig. 3C). A complex of Oct4 and Sox2 activates all three genes [23, 50, 59] and a complex of Oct4 and the Nanog-dimer activates *Oct4* and *Nanog* [48, 60]. We represent these regulations as

$$\begin{aligned} x_1 &= x_3 = \frac{h_0 p_1 p_2}{h_0 p_1 p_2 + f_0} \frac{h_1 p_1 p_3^2}{h_1 p_1 p_3^2 + f_1}, \\ x_2 &= \frac{h_0 p_1 p_2}{h_0 p_1 p_2 + f_0}. \end{aligned} \quad (16)$$

We use $\omega = \omega_1 = \omega_2 = \omega_3$ at the beginning, but we assume the heterogeneous ω_i later to compare the simulated data with the experimental results. For simplicity, we assume that the other parameters do not depend on i . We write $\bar{p} = \xi_{11}$.

[1] G. Nicoletti and D. M. Busiello, Information propagation in multilayer systems with higher-order interactions

across timescales, Phys Rev X **14**, 021007 (2024).

TABLE II. Parameters used in each circuit

Parameters	Circuit A	Circuit B	Circuit C
Coefficients used in $\bar{r}_i^{yy'}(x_i) = \mu^{yy'} + \gamma^{yy'} x_i$ (Eq. 3)	$\mu^{yy'}$	k	k
determining the transition rate from a histone state y' to the other y	γ^{0-1}	$0.6k$	$-0.6k$
	γ^{10}	$0.6k$	$-0.6k$
	γ^{01}	$-0.6k$	$0.6k$
	γ^{-10}	$-0.6k$	$0.6k$
TF binding/unbinding parameter ratio	h_0/f	10	10
	h_1/f	-	100
Normalized protein-synthesis rate $\xi_{xy} = g_{xy}/(k\Omega)$	ξ_{11}	\bar{p}	0.2
at the TF-binding state x	ξ_{01}	0.2	\bar{p}
and the histone state y	ξ_{10}	0.2	0
	ξ_{00}	0	0.2
	ξ_{1-1}	0	0
	ξ_{0-1}	0	0

TABLE III. Parameters in the deep epigenetic regulation model

Coefficients used in	ν^{0-1}	0	Coefficients used in	μ^{0-1}	0
$\bar{s}^{zz'} = \nu^{zz'} + \sigma_x^{zz'} x_i + \sigma_y^{zz'} y_{i+}$ (Eq. 11)	ν^{10}	k	$\bar{r}^{yy'} = \mu^{yy'} + \gamma_x^{yy'} x_i + \gamma_z^{yy'} z_{i+}$ (Eq. 12)	μ^{10}	k
determining the transition rate	ν^{01}	k	determining the transition rate	μ^{01}	k
from a chromatin structure z' to the other z	ν^{-10}	$2k$	from a histone state y' to the other y	μ^{-10}	$2k$
	σ_x^{0-1}	$0.8k$		γ_x^{0-1}	$0.8k$
	σ_x^{10}	$0.8k$		γ_x^{10}	$0.8k$
	σ_x^{01}	$-0.8k$		γ_x^{01}	$-0.8k$
	σ_x^{-10}	$-0.8k$		γ_x^{-10}	$-0.8k$
	σ_y^{0-1}	$0.2k$		γ_z^{0-1}	$0.2k$
	σ_y^{10}	$0.2k$		γ_z^{10}	$0.2k$
	σ_y^{01}	$-0.2k$		γ_z^{01}	$-0.2k$
	σ_y^{-10}	$-0.2k$		γ_z^{-10}	$-0.2k$
TF binding/unbinding parameter ratio	h_0/f	10			
	h_1/f	100			
Normalized protein-synthesis rate		$\xi(1, 1) \quad \bar{p}$	$\xi(1, 0) \quad 0.2$		$\xi(1, -1) \quad 0$
$\xi(x, z) = g(x, z)/(k\Omega)$		$\xi(0, 1) \quad 0.2$	$\xi(0, 0) \quad 0$		$\xi(0, -1) \quad 0$

- [2] C. J. Honey, R. Kötter, M. Breakspear, and O. Sporns, Network structure of cerebral cortex shapes functional connectivity on multiple time scales, *Proc Natl Acad Sci U S A* **104**, 10240 (2007).
- [3] A. Hastings, Timescales, dynamics, and ecological understanding, *Ecology* **91**, 3471 (2010).
- [4] B. Mélykúti, J. P. Hespanha, and M. Khammash, Equilibrium distributions of simple biochemical reaction systems for time-scale separation in stochastic reaction networks, *J R Soc Interface* **11**, 20140054 (2014).
- [5] D. Senkowski and A. K. Engel, Multi-timescale neural dynamics for multisensory integration, *Nat Rev Neurosci* **25**, 625 (2024).
- [6] E. Ela and M. O'Malley, Studying the variability and uncertainty impacts of variable generation at multiple timescales, *IEEE Transactions on Power Systems* **27**, 1324 (2012).
- [7] M. Sasai and P. G. Wolynes, Stochastic gene expression as a many-body problem, *Proc Natl Acad Sci U S A* **100**, 2374 (2003).
- [8] A. M. Walczak, J. N. Onuchic, and P. G. Wolynes, Absolute rate theories of epigenetic stability, *Proc Natl Acad Sci U S A* **102**, 18926 (2005).
- [9] P.-Z. Shi and H. Qian, A perturbation analysis of rate theory of self-regulating genes and signaling networks, *J Chem Phys* **127**, 065104 (2011).
- [10] J. E. M. Hornos, D. Schultz, G. C. P. Innocentini, J. Wang, A. M. Walczak, J. N. Onuchic, and P. G. Wolynes, Self-regulating gene: an exact solution, *Phys Rev E* **72**, 051907 (2005).
- [11] K. Zhang, M. Sasai, and J. Wang, Eddy current and coupled landscapes for nonadiabatic and nonequilibrium complex system dynamics, *Proc Natl Acad Sci U S A* **110**, 14930 (2013).
- [12] C. Chen, K. Zhang, H. Feng, M. Sasai, and J. Wang, Multiple coupled landscapes and non-adiabatic dynamics with applications to self-activating genes, *Phys Chem Chem Phys* **17**, 29036 (2015).
- [13] B. Bhattacharyya, J. Wang, and M. Sasai, Stochastic epigenetic dynamics of gene switching, *Phys Rev E* **102**,

- 042408 (2020).
- [14] G. Tkačik and A. M. Walczak, Information transmission in genetic regulatory networks: a review, *J Phys Condens Matter* **23**, 153102 (2011).
 - [15] J. Elf, G. W. Li, and X. S. Xie, Probing transcription factor dynamics at the single-molecule level in a living cell, *Science* **316**, 1191 (2007).
 - [16] H. Zheng, P. Y. Ho, M. Jiang, B. Tang, W. Liu, D. Li, X. Yu, N. E. Kleckner, A. Amir, and C. Liu, Interrogating the *Escherichia coli* cell cycle by cell dimension perturbations, *Proc Natl Acad Sci U S A* **113**, 15000 (2016).
 - [17] X. Fang, Q. Liu, C. Bohrer, Z. Hensel, W. Han, J. Wang, and J. Xiao, Cell fate potentials and switching kinetics uncovered in a classic bistable genetic switch, *Nat Commun* **9**, 2787 (2018).
 - [18] Z. Jiang, L. Tian, X. Fang, K. Zhang, Q. Liu, Q. Dong, E. Wang, and J. Wang, The emergence of the two cell fates and their associated switching for a negative auto-regulating gene, *BMC Biol* **17**, 49 (2019).
 - [19] D. Schultz, E. Ben Jacob, J. N. Onuchic, and P. G. Wolynes, Molecular level stochastic model for competence cycles in *Bacillus subtilis*, *Proc Natl Acad Sci U S A* **104**, 17582 (2007).
 - [20] I. Golding, J. Paulsson, S. M. Zawilski, and E. C. Cox, Real-time kinetics of gene activity in individual bacteria, *Cell* **123**, 1025 (2005).
 - [21] N. A. Hathaway, O. Bell, C. Hodges, E. L. Miller, D. S. Neel, and G. R. Crabtree, Dynamics and memory of heterochromatin in living cells, *Cell* **149**, 1447 (2012).
 - [22] L. Bintu, J. Yong, Y. E. Antebi, K. McCue, Y. Kazuki, N. Uno, M. Oshimura, and M. B. Elowitz, Dynamics of epigenetic regulation at the single-cell level, *Science* **351**, 720 (2016).
 - [23] J. L. Chew, Y. H. Loh, W. Zhang, X. Chen, W. L. Tam, *et al.*, Reciprocal transcriptional regulation of Pou5f1 and Sox2 via the Oct4/Sox2 complex in embryonic stem cells, *Mol Cell Biol* **25**, 6031 (2005).
 - [24] M. Thomson, S. J. Liu, L. N. Zou, Z. Smith, A. Meissner, *et al.*, Pluripotency factors in embryonic stem cells regulate differentiation into germ layers, *Cell* **145**, 875 (2011).
 - [25] M. Sasai, Y. Kawabata, K. Makishi, K. Itoh, and T. P. Terada, Time scales in epigenetic dynamics and phenotypic heterogeneity of embryonic stem cells, *PLoS Comput Biol* **9**, e1003380 (2013).
 - [26] S. S. Ashwin and M. Sasai, Effects of collective histone state dynamics on epigenetic landscape and kinetics of cell reprogramming, *Sci Rep* **5**, 16746 (2015).
 - [27] X.-J. Tiana, H. Zhang, J. Sannerud, and J. Xing, Enhancer dynamics: Unraveling the mechanism of transcriptional bursting, *Proc Natl Acad Sci U S A* **113**, E2889 (2016).
 - [28] N. Folguera-Blasco, R. Pérez-Carrasco, E. Cuyás, J. A. Menendez, and T. Alarcón, A multiscale model of epigenetic heterogeneity-driven cell fate decision-making, *PLoS Comput Biol* **15**, e1006592 (2019).
 - [29] J. Chen, Z. Zhang, L. Li, B. C. Chen, A. Revyakin, B. Hajj, W. Legant, M. Dahan, T. Lionnet, E. Betzig, R. Tjian, and Z. Liu, Single-molecule dynamics of enhanceosome assembly in embryonic stem cells, *Cell* **156**, 1274 (2014).
 - [30] M. Mazzocca, E. Colombo, A. Callegari, and D. Mazza, Transcription factor binding kinetics and transcriptional bursting: What do we really know?, *Curr Opin Str Biol* **71**, 239 (2021).
 - [31] T. Fukaya, Enhancer dynamics: Unraveling the mechanism of transcriptional bursting, *Sci Adv* **9**, eadj3366 (2023).
 - [32] E. A. Leyes Porello, R. T. Trudeau, and B. Lim, Transcriptional bursting: stochasticity in deterministic development, *Development* **150**, dev201546 (2023).
 - [33] J. V. W. Meeussen and T. L. Lenstra, Time will tell: comparing timescales to gain insight into transcriptional bursting, *Trends Genet* **40**, 160 (2024).
 - [34] T. Misteli, The self-organizing genome: Principles of genome architecture and function, *Cell* **183**, 28 (2020).
 - [35] A. J. Bannister and T. Kouzarides, Regulation of chromatin by histone modifications, *Cell Res* **21**, 381 (2011).
 - [36] K. Maeshima, K. Kaizu, S. Tamura, T. Nozaki, T. Kokubo, and K. Takahashi, The physical size of transcription factors is key to transcriptional regulation in chromatin domains, *J Phys Cond Matter* **27**, 064116 (2015).
 - [37] I. B. Dodd, M. A. Micheelsen, K. Sneppen, and G. Thon, Theoretical analysis of epigenetic cell memory by nucleosome modification, *Cell* **129**, 813 (2007).
 - [38] H. Zhang, X. J. Tian, A. Mukhopadhyay, K. S. Kim, and J. Xing, Statistical mechanics model for the dynamics of collective epigenetic histone modification, *Phys Rev Lett* **112**, 068101 (2014).
 - [39] E. J. Chory, J. P. Calarco, N. A. Hathaway, O. Bell, D. S. Neel, and G. R. Crabtree, Nucleosome turnover regulates histone methylation patterns over the genome, *Mol Cell*, 61 (2019).
 - [40] A. Sood and B. Zhang, Quantifying epigenetic stability with minimum action paths, *Phys Rev E* **101**, (2020).
 - [41] A. Mayran and J. Drouin, Pioneer transcription factors shape the epigenetic landscape, *J Biol Chem* **293**, 13795 (2018).
 - [42] S. Henikoff and S. A., Histone modification: cause or cog?, *Trends Genet* **27**, 389 (2011).
 - [43] M. Ptashne, Epigenetics: core misconception, *Proc Natl Acad Sci U S A* **110**, 7101 (2013).
 - [44] A. M. Miangolarra, D. S. Saxton, Z. Yan, J. Rine, and M. Howard, Two-way feedback between chromatin compaction and histone modification state explains *Saccharomyces cerevisiae* heterochromatin bistability, *Proc Natl Acad Sci U S A* **121**, e2403316121 (2024).
 - [45] J. Wang, L. Xu, and E. Wang, Potential landscape and flux framework of nonequilibrium networks: Robustness, dissipation, and coherence of biochemical oscillations, *Proc Natl Acad Sci U S A* **105**, 12271 (2008).
 - [46] H. Feng and J. Wang, Potential and flux decomposition for dynamical systems and non-equilibrium thermodynamics: Curvature, gauge field, and generalized fluctuation-dissipation theorem, *J Chem Phys* **135**, 234511 (2011).
 - [47] X. Fang, K. Kruse, T. Lu, and J. Wang, Nonequilibrium physics in biology, *Rev Mod Phys* **91**, 045004 (2019).
 - [48] J. Wang, S. Rao, J. Chu, X. Shen, D. N. Levasseur, *et al.*, A protein interaction network for pluripotency of embryonic stem cells, *Nature* **444**, 364 (2006).
 - [49] J. R. Boyer LA, Mathur D, Molecular control of pluripotency, *Curr Opin Genet Dev* **16**, 455 (2006).
 - [50] H. Niwa, How is pluripotency determined and maintained, *Development* **134**, 635 (2007).

- [51] P. Navarro, 2i, or not 2i: The soliloquy of nanog-negative mouse embryonic stem cells, *Stem Cell Reports* **11**, 1 (2018).
- [52] A. M. Singh, T. Hamazaki, E. Katherine, N. T. Hankowski, and T. N., A heterogeneous expression pattern for nanog in embryonic stem cells, *Stem Cells* **25**, 2534 (2007).
- [53] T. Kalmar, C. Lim, P. Hayward, S. Munõz Descalzo, J. Nichols, *et al.*, Regulated fluctuations in nanog expression mediate cell fate decisions in embryonic stem cells, *PLoS Biol* **7**, e1000149 (2009).
- [54] M. A. Canham, A. A. Sharov, M. S. H. Ko, and J. M. Brickman, Functional heterogeneity of embryonic stem cells revealed through translational amplification of an early endodermal transcript, *PLoS Biol* **8**, e1000379 (2010).
- [55] L. Hyslop, M. Stojkovic, L. Armstrong, T. Walter, P. Stojkovic, S. Przyborski, M. Herbert, A. Murdoch, T. Strachan, and M. Lako, Downregulation of nanog induces differentiation of human embryonic stem cells to extraembryonic lineages, *Stem Cells* **23**, 1035 (2005).
- [56] P. Yu, Q. Nie, C. Tang, and L. Zhang, Nanog induced intermediate state in regulating stem cell differentiation and reprogramming, *BMC Syst Biol* **12**, 22 (2018).
- [57] T. Samanta and S. Kar, Dynamical reorganization of transcriptional events governs robust nanog heterogeneity, *J Phys Chem B* **123**, 5246 (2019).
- [58] P. Navarro, N. Festuccia, D. Colby, A. Gagliardi, *et al.*, Oct4/Sox2-independent Nanog autorepression modulates heterogeneous nanog gene expression in mouse es cells, *EMBO J* **24**, 4547 (2012).
- [59] S. Masui, Y. Nakatake, Y. Toyooka, D. Shimosato, R. Yagi, *et al.*, Pluripotency governed by Sox2 via regulation of Oct3/4 expression in mouse embryonic stem cells, *Nat Cell Biol* **9**, 625 (2007).
- [60] Y. H. Loh, Q. Wu, J. L. Chew, V. B. Vega, W. Zhang, *et al.*, The oct4 and nanog transcription network regulates pluripotency in mouse embryonic stem cells, *Nat Genet* **38**, 431?440 (2006).
- [61] E. Calo and J. Wysocka, Modification of enhancer chromatin: what, how, and why?, *Mol Cell* **49**, 825 (2013).
- [62] S. I. S. Grewal, The molecular basis of heterochromatin assembly and epigenetic inheritance, *Mol Cell* **83**, 1767 (2023).
- [63] E. de Wit, B. Bouwman, Y. Zhu, *et al.*, The pluripotent genome in three dimensions is shaped around pluripotency factor, *Mol Cell* **501**, 227 (2013).
- [64] D. Lando, X. Ma, Y. Cao, *et al.*, Enhancer-promoter interactions are reconfigured through the formation of long-range multiway hubs as mouse ES cells exit pluripotency, *Mol Cell* **84**, 1406 (2024).
- [65] R. Stadhouders, E. Vidal, F. Serra, *et al.*, Transcription factors orchestrate dynamic interplay between genome topology and gene regulation during cell reprogramming, *Nat Genet* **50**, 238 (2018).
- [66] H. Miura, S. Takahashi, R. Poonperm, *et al.*, Single-cell DNA replication profiling identifies spatiotemporal developmental dynamics of chromosome organization, *Nat Genet* **51**, 1356 (2019).
- [67] Z. Liu, Y. Chen, Q. Xia, *et al.*, Linking genome structures to functions by simultaneous single-cell Hi-C and RNA-seq, *Science* **380**, 1070 (2023).
- [68] N. Masuda, K. Aihara, and N. G. MacLaren, Anticipating regime shifts by mixing early warning signals from different nodes, *Nat Commun* **15**, 1086 (2024).
- [69] K. Maehara and Y. Ohkawa, Modeling latent flows on single-cell data using the Hodge decomposition, *bioRxiv*, <https://doi.org/10.1101/592089> (2019).
- [70] X. Qiu, Y. Zhang, J. D. Martin-Rufino, C. Weng, S. Hosseinzadeh, D. Yang, A. N. Pogson, M. Y. Hein, K. Hoi Joseph Min, L. Wang, E. I. Grody, M. J. Shurtleff, R. Yuan, S. Xu, Y. Ma, J. M. Replogle, E. S. Lander, S. Darmanis, I. Bahar, V. G. Sankaran, J. Xing, and J. S. Weissman, Mapping transcriptomic vector fields of single cells, *Cell* **185**, 690 (2022).
- [71] Z. Su, Y. Tong, and G.-W. Wei, Hodge decomposition of single-cell RNA velocity, *Journal of Chemical Information and Modeling* **64**, 3558 (2024).
- [72] L. Zhu, S. Yang, K. Zhang, H. Wang, X. Fang, and J. Wang, Uncovering underlying physical principles and driving forces of cell differentiation and reprogramming from single-cell transcriptomics, *Proc Natl Acad Sci U S A* **121**, e2401540121 (2024).
- [73] U. Alon, Network motifs: theory and experimental approaches, *Nat Rev Genet* **8**, 450 (2007).
- [74] Z. Zhou, Y. Liu, Y. Feng, S. Klepin, L. S. Tsimring, L. Pillus, J. Hasty, and N. Hao, Engineering longevity-design of a synthetic gene oscillator to slow cellular aging, *Science* **380**, 376 (2023).